Label-Free, Quantitative Imaging of MoS_2-Nanosheets in Live Cells with Simultaneous Stimulated Raman Scattering and Transient Absorption Microscopy

Lili Zhang, Sida Shen, Zhuang Liu, and Minbiao Ji**

Probing nanoparticle–cell interactions in vivo plays a key role in the research and development of nanomedicine and nano-biophotonics. However, simultaneously imaging nanoparticles and intracellular biomolecules in a label-free manner has been a challenge, especially for the majority of nanoparticles that do not emit one- or two-photon excited fluorescence. In this work, a strong optical transient absorption (TA) signal is observed for synthesized MoS_2 nanosheets that could be used for sensitive and quantitative imaging of their intracellular distributions. Furthermore, a dual-modal microscopy technique is developed to simultaneously image MoS_2 with TA microscopy and cellular lipids/proteins with stimulated Raman scattering (SRS) microscopy. This technique is based on precise pulse engineering and dual-phase lock-in detection. Its capability to quantify the uptake dynamics of MoS_2 into live HeLa cells is demonstrated and the colocalization of MoS_2 nanosheets with intracellular lipid rich organelles is observed. Different sized MoS_2 nanosheets are found to have distinct uptake dynamics as well as transient photocarrier dynamics. These results indicate that dual-modal SRS/TA microscopy may provide a general solution for investigating a large variety of nanomaterials that absorb light but do not fluoresce.

1. Introduction

Novel pump–probe based nonlinear optical microscopies have been developed to image the intrinsic properties of molecules and nanoparticles, especially those that hardly fluoresce. These techniques include stimulated Raman scattering (SRS) microscopy,[1] stimulated emission (SE) microscopy,[2] transient absorption (TA) microscopy,[3] and ground-state bleaching microscopy.[4] SRS microscopy is an emerging label-free chemical imaging technique based on the vibrational spectroscopy of biomolecules, such as lipids, proteins, and DNA.[5–8] It has been successfully applied to various biomedical studies, including those focused brain tumor detection,[9–11] lipid metabolism,[12,13] drug delivery, and quantitative chemical analysis.[6,14] TA microscopy detects the differential absorption of a probe beam induced by the pump excitation, which creates short-lived photocarriers or excited electronic states. It has been used to image numerous nanomaterials, including gold nanoparticles,[15–19] nanodiamonds,[20] single-wall carbon nanotubes,[21–23] graphene,[24–26] and graphene oxide.[27,28] However, no single label-free imaging method can detect biomolecules and nanoparticles simultaneously, largely because detecting these two species involves different optical processes and requires different laser sources or settings. Previous SE and TA studies were designed to intentionally avoid interference from the SRS process.[18] By contrast, we have developed a microscope modality that, with the proper choice of nanomaterials, can image nanoparticles and cells simultaneously by taking advantage of their different transient optical properties under the same laser settings.

Fluorescence labeling methods, which are widely used in biological studies,[29–33] can be used to observe the interactions between nanomaterials and biological systems by attaching fluorescent molecules onto target nanoparticles.[34–36] Examples of this include the study of drug delivery by nanoparticles in live cells,[37–39] cellular uptake and transport of short interfering RNA (siRNA),[40,41] and accumulation of drugs carried by functional nanomaterials around tumor tissues.[42] However, labeling methods suffer from several drawbacks, such as the complexity of staining process, nonspecific and unstable labeling, and photobleaching. More importantly, fluorescence based methods are ill-suited at providing direct and quantitative measures of the labeled nanoparticles. Although atomic resolution microscopy techniques such as transmission electron microscopy are able to characterize intracellular nanoparticles in great detail, they does not work for living systems.[41] For light-absorbing nanoparticles, photoacoustic microscopy can image them with decent sensitivity and imaging depth in vivo,[43] but it lacks the high spatial resolution needed to visualize the intracellular behavior of these nanoparticles. Thus, label-free

---

L. Zhang, Prof. M. Ji
State Key Laboratory of Surface Physics and Department of Physics
Collaborative Innovation Center of Genetics and Development
School of Life Sciences
Fudan University
Shanghai 200433, China
E-mail: minbiaoj@fudan.edu.cn

S. Shen, Prof. Z. Liu
Institute of Functional Nano & Soft Materials (FUNSOM)
Collaborative Innovation Center of Suzhou
Nano Science and Technology
Soochow University
Suzhou, Jiangsu 215123, China
E-mail: zliu@suda.edu.cn

DOI: 10.1002/adbi.201700013

optical imaging methods capable of the sensitive detection of nanoparticles in living cells could fill in the existing gaps in this field and enable in vivo studies with subcellular resolution.

Transition metal dichalcogenides (TMDCs) have recently been shown to demonstrate excellent electrical, optical, and chemical properties and have been extensively investigated in both fundamental studies and device fabrication.[44] As a typical TMDC, molybdenum disulfide (MoS_2) nanosheets have shown great potential for applications in the biomedical field, such as drug delivery,[45] photodynamic therapy,[46] photothermal therapy,[47] and photoacoustic imaging of tumors.[43] This is mainly due to the unique optical properties of MoS_2 nanosheets, particularly their high absorbance in the near-infrared (NIR) region. However, unlike few-layered MoS_2, these nanosheets do not generate detectable one- or two-photon fluorescence or emit second harmonic generation photons.[44,48] To the best of our knowledge, label-free optical imaging of MoS_2 nanosheets has not yet been reported.

In this work, we found that MoS_2 nanosheets could generate a strong nonlinear optical TA signal in the NIR region, partially due to their high linear absorption. Thus, the same laser source could be used for both TA and SRS microscopies. Because the temporal features of TA and SRS differ significantly, acquiring data at multiple delay times could be used to separate them. Moreover, using precise pulse engineering we have developed a method to simultaneously image MoS_2 (TA) and cells (SRS) with dual-phase lock-in detection. This parallel dual-modal imaging technique allows the quantitative study of nanoparticle internalization dynamics and colocalization of MoS_2 with lipid rich organelles, which is difficult to achieve with conventional sequential multimodal imaging methods.

2. Results and Discussion

2.1. Synthesis and Characterization of MoS_2 Nanosheets

Samples of three different sized MoS_2 nanosheets were synthesized. The Morrison method was used to synthesize larger-sized PEG (polyethylene glycol) functionalized nanosheets,[47] and a modified bottom-up procedure was used to synthesize smaller-sized GSH (glutathione)-functionalized nanosheets.[49] Detailed protocols and parameters can be found in the Experimental Section. We used dynamic light scattering to characterize the size of MoS_2 nanosheets. As shown in **Figure 1**, the as-made chemically exfoliated MoS_2-PEG nanosheets showed an average diameter of ≈90 nm, and the MoS_2-GSH nanosheets synthesized using the modified bottom-up procedure for different durations of time showed average diameters of ≈20 and ≈6 nm. Vis–NIR absorption spectra of MoS_2 showed strong visible to NIR absorption with significant size dependence (Figure 1d). In particular, the NIR absorbance of large-sized MoS_2-PEG is much stronger than that of MoS_2-GSH with smaller sizes, and the absorbance of MoS_2-GSH also decreased slightly as size decreased (Figure 1d). Such size-dependent optical absorption of nanoparticles has been reported previously.[50]

2.2. Dual-Modal SRS/TA Microscopy

The design of our dual-modal SRS/TA microscope is illustrated in **Figure 2**, which is upgraded from our previous apparatus of two-color SRS microscope.[51] In this setup, pulsed femtosecond laser beams from a commercial OPO (Optical

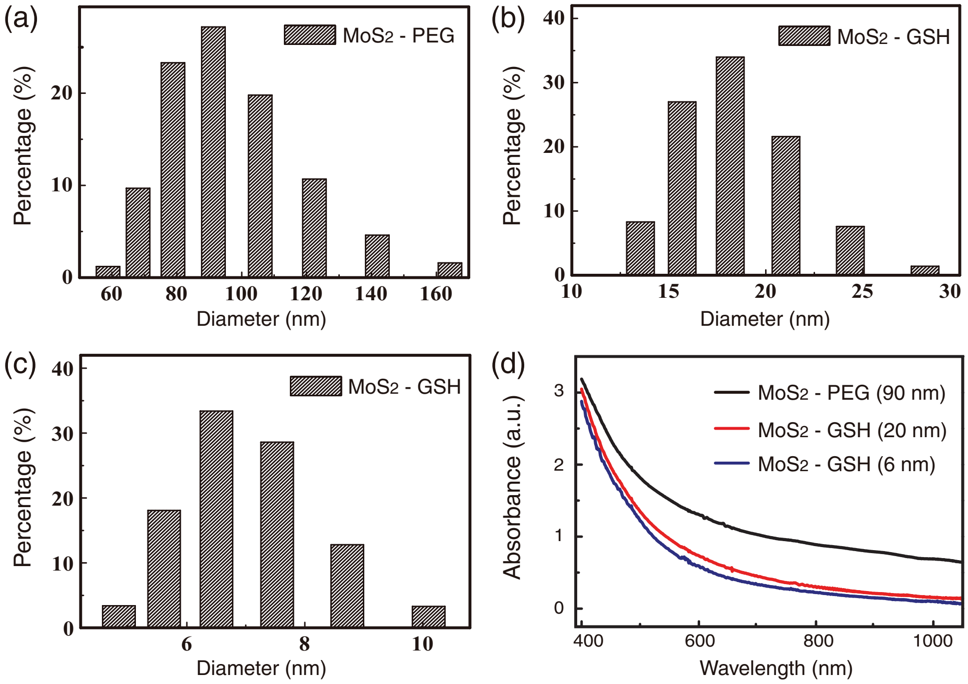

Figure 1. Characterization of MoS_2 nanosheets. Dynamic light scattering results show the sizes of different nanosheets samples: a) MoS_2-PEG with a mean size of ≈90 nm, b) MoS_2-GSH with a mean size of ≈20 nm, and c) MoS_2-GSH with a mean size of ≈6 nm. d) Vis–NIR absorption spectra of the three samples.

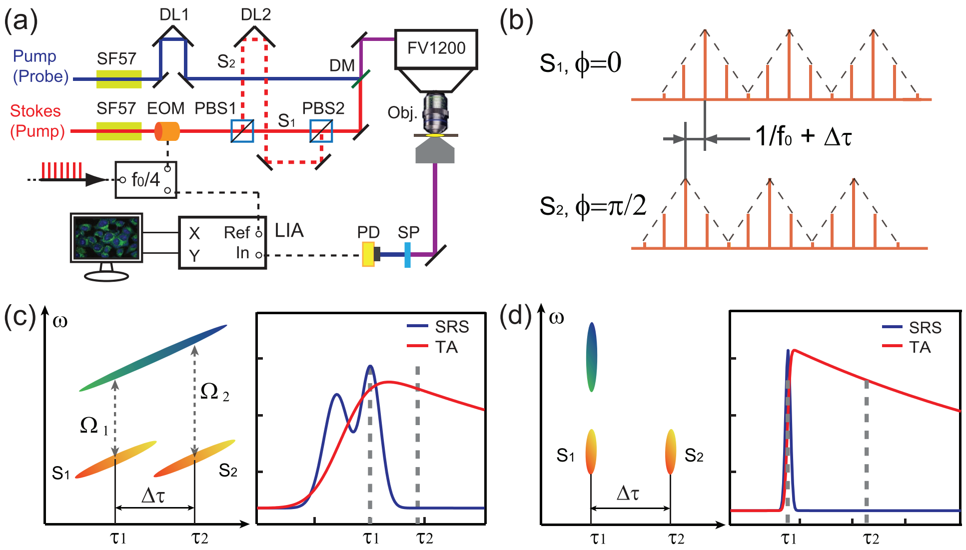

Figure 2. Illustration of dual-modal SRS/TA microscopy. a) Optical layouts. DL, delay line; EOM, electro-optical modulator; PBS, polarizing beam splitter; DM, dichroic mirror; SP, short pass filter; PD, photodiode; LIA, lock-in amplifier. b) Pulse trains of the dual Stokes beams S_1 and S_2 modulated with a $\pi/2$ phase difference. c) Temporal profiles of the chirped pump (blue) and two Stokes (orange) pulses, showing high spectral resolution for SRS and low temporal resolution for TA. d) Temporal profiles of the nonchirped pulses, showing low spectral resolution for SRS and high temporal resolution for TA.

Parametric Oscillator) laser (Insight DS+, Newport, CA) were used as the laser source. The fundamental 1040 nm laser was used as the Stokes beam for SRS and the pump beam for TA, while the tunable OPO output (690–1300 nm) served as the pump beam for SRS and the probe beam for TA. The intensity of the 1040 nm beam was modulated at 1/4 of the laser pulse repetition rate ($f_0 = 80$ MHz) using a frequency divider and an electro-optical modulator (EOM). The two laser beams were combined through a dichromic mirror, spatially and temporally overlapped, delivered into the laser-scanning microscope (FV 1200, Olympus) and focused onto the samples. The stimulated Raman loss and TA signal generated were optically filtered, detected by a back-biased photodiode and demodulated with a lock-in amplifier (LIA) (HF2LI, Zurich Instruments) to feed the analog input of the microscope to form images.

Hyper-spectral SRS was configured to function in "spectral focusing" mode,[52] which involves the insertion of highly dispersive glass rods (SF 57, 78 cm long) to chirp pulses to several picoseconds (pump: ≈3.8 ps, Stokes: ≈1.8 ps). Using matched linear chirps, SRS spectra could be realized by scanning the optical delay line (DL1), as shown in Figure 2c. This method effectively projects time domain information onto the spectral domain, enabling spectral acquisition without tuning laser wavelengths, which is critical for the design of dual-modal SRS/TA microscopy. To achieve parallel two-channel imaging, we built a Mach–Zehnder-type interferometer of the 1040 nm beam, creating two arms (S_1 and S_2) between two polarizing beam splitters (PBS1 and PBS2). A second delay line (DL2) was set to adjust the time delay between S_1 and S_2. Notice that S_1 and S_2 were modulated in antiphase at 20 MHz right after PBS1; but after we added a time delay of one pulse interval ($T_0 = 12.5$ ns) to DL2, the modulation phase was shifted to $\pi/2$ (Figure 2b), while the signal intensity remained the same. The combination of DL1 and DL2 allows full control of the delay profile of the three beams. By choosing τ_1 and τ_2 properly, SRS signals at corresponding Raman frequencies Ω_1 and Ω_2 could be generated simultaneously in the pump beam but with a $\pi/2$ phase difference.[51]

TA signals could be detected in the same setup, with the transient dynamics revealed by scanning DL1 as well. Therefore, the measured time-resolved data served as the spectra for SRS and at the same time appeared as the transient dynamics curve for TA. In other words, the TA curve could be treated as the "spectral" signature of MoS_2, which is drastically different from the SRS spectra of lipids/proteins (Figure 2c). These spectral differences allow the separation of the two via a linear decomposition algorithm.[6,52] With the dual-beam setup, the detected signal (S_{tot}) is a superposition of the two sources at delays τ_1 and τ_2

$$S_{\text{tot}}(t) = S(\tau_1)\sin\left(\frac{\pi f_0 t}{2} + \phi_0\right) + S(\tau_2)\cos\left(\frac{\pi f_0 t}{2} + \phi_0\right) \quad (1)$$

Thus, transient signals $S(\tau_1)$ and $S(\tau_2)$ could be simultaneously demodulated through the in-phase (X) and quadrature (Y) output channels of the phase-sensitive LIA with the proper setting of reference phase ϕ_0. By choosing τ_1 and τ_2 carefully so that $S(\tau_2)$ represents TA and $S(\tau_1)$ represents SRS or a combination of SRS and TA (Figure 2c), we then could achieve parallel SRS/TA imaging without the need for adjusting laser wavelength or any other experimental parameters.

In addition, we could bypass the SF57 glass rods and convert the system into a femtosecond version to achieve high temporal resolution for TA, although the spectral resolution of SRS would be lost (Figure 2d). This flexibility could be used to meet additional experimental needs in cases where finer time resolution is more critical than spectral information. Detailed characterization and evaluation of the interference and cross-talk effects have been investigated previously[51] and indicate the robustness of the technique as a dual-modal imaging method.

2.3. Transient Absorption Dynamics of MoS_2 Nanosheets

We studied the transient dynamics of the three different sized colloidal MoS_2 nanosheets samples with the femtosecond version of the system to maintain a sufficient time resolution (≈250 fs). A pump wavelength of 1040 nm and probe wavelength of 802 nm were used throughout the experiments. Representative TA images of MoS_2 nanosheets in solution are shown in **Figure 3**a. Transient dynamics were measured by scanning DL1 frame by frame with a step size of 0.067 ps. Size-dependent decay curves were measured and are shown in Figure 3b, and the negative sign of $\Delta T/T$ indicated increased absorption of the probe beam induced by pump excitation. The overall carrier dynamics were composed of multiple time scales, including a rapid sub-picosecond decay, most likely associated with ultrafast exciton formation from hot carriers and Auger recombination,[53] and a slower decay on a several picosecond timescale, which agrees quite well with the exciton lifetime of layered MoS_2.[54] The large MoS_2-PEG sample contains an additional long lifetime component on the order of tens of picoseconds. We fitted the decay curves with multiexponential decay functions, and the results are shown in **Table 1**. There appears to be a trend of larger-sized MoS_2 nanosheets having shorter exciton lifetimes, which is related to the quantum confinement effect of small nanocrystals;[55] however, the underlying physics of this effect is not the focus of this work.

We then measured the power dependence of the TA signal at a fixed time delay. A linear relationship was observed at each pump and probe laser powers (Figure 3c; Figure S1, Supporting Information), indicating the third-order optical nonlinearity of the process. We next verified the linear dependence of TA signal intensity on particle concentration with fixed laser intensity and time delay (Figure 3d; Figure S1, Supporting Information). This linear concentration dependence plays an important role in quantitative analysis and can be used to study the uptake dynamics and efficiency of MoS_2 nanosheets into cells. Notice that both the power and concentration dependences of TA behave exactly the same as those of the SRS signal. Thus, the unified equation for the TA and SRS signals could be written as $S = C\chi^{(3)}I_1I_2$ where C is the molecule/particle concentration, $\chi^{(3)}$ is the third-order optical susceptibility, and I corresponds to each of the two laser beam intensities.

2.4. Imaging MoS_2 Nanosheets Uptake in Live HeLa Cells

To selectively image intracellular lipids, proteins, and MoS_2, we converted the system to the picosecond version with the glass rods (Figure 2a) to enable hyperspectral imaging. We first calibrated the system with standard test chemicals of lipids (oleic acid, OA), proteins (bovine serum albumin, BSA), and MoS_2 nanosheets. Spontaneous Raman spectra of lipids/proteins are shown in **Figure 4**a, and their SRS spectra are shown in Figure 4b, along with the TA curve of MoS_2. These “spectra” reveal the differences between the chemical components of these species that allow their differentiation. In contrast to the typical Raman bands of lipids/proteins in the CH stretch

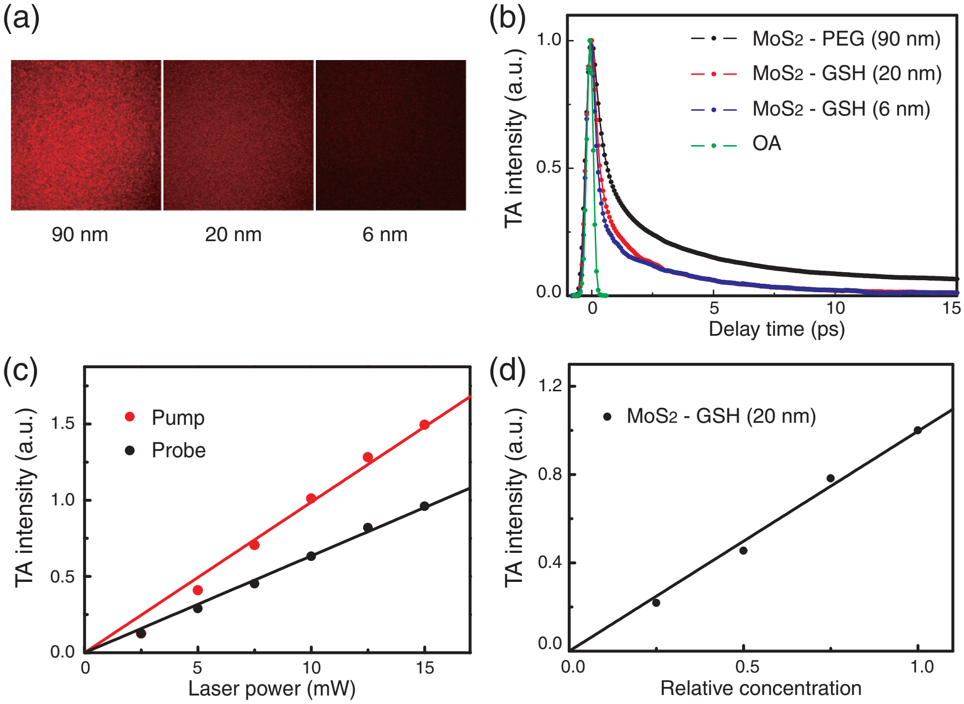

Figure 3. Nonlinear optical transient absorption (TA) of MoS_2 nanosheets. a) TA images of MoS_2 nanosheets in solutions. b) Size-dependent time-resolved TA dynamics of MoS_2 nanosheets. c) Measurements of the linear dependence of TA intensity on the laser power of the pump or probe beam and d) on the MoS_2 concentration in solution.

Table 1. Transient absorption dynamics of MoS_2 nanosheets fitted with multiexponential decay. Tri-exponential for MoS_2-PEG: $I = A_1{*}\exp(-t/T_1) + A_2{*}\exp(-t/T_2) + A_3{*}\exp(-t/T_3)$, and bi-exponential for MoS_2-GSH: $I = A_1{*}\exp(-t/T_1) + A_2{*}\exp(-t/T_2)$.

	MoS_2-PEG	MoS_2-GSH	
	(90 nm)	(20 nm)	(6 nm)
T_1 [ps]	0.46	0.42	0.41
A_1	0.63	0.72	0.64
T_2 [ps]	3.36	3.89	4.55
A_2	0.33	0.23	0.19
T_3 [ps]	46.92		
A_3	0.08		

region, MoS_2 shows asymmetric transient behavior resulting from the broadening of the previous femtosecond transient dynamics (Figures 3b and 4b). Both the TA signal of MoS_2 and SRS signal of lipids/proteins decay away at $\tau < -6$ ps when the probe pulse is ahead of the pump pulse. While the SRS signal of lipids/proteins rapidly vanishes within 2 ps (Figure 4b), the TA signal of MoS_2 persists for at least 10 ps (Figure 3b). Thus, by varying the time delay (DL1), we could achieve "multicolor" images of HeLa cells incubated with MoS_2 nanosheets. At $\tau = 2.5$ ps, the image is primarily distributed MoS_2 (Figure 4c, first row); at $\tau = 0$ ps, the signal is mainly contributed from lipids and MoS_2 (Figure 4c, second row); and at $\tau = -2.2$ ps, the signal is a combination of lipids, proteins, and MoS_2 (Figure 4c, third row). As a control, HeLa cells without MoS_2 only displayed signals for their lipid and protein contents (Figure S2 of the Supporting Information, 0 h). In contrast to the even distribution of MoS_2 nanosheets in solution (Figure 3a), intracellular MoS_2 nanosheets mainly exist as small aggregates. This aggregation may be related to the internalization mechanisms and intracellular fate of MoS_2; for example, it could be wrapped in endosome during clathrin-mediated endocytosis or micropinocytosis and stored in lysosomes for decomposition and further exocytosis.[40,41] In addition, we observed that most MoS_2 nanosheets were distributed in the cytoplasm, especially in the perinuclear region, after 4 h of incubation but were absent inside the nucleus (Figure 4c; Figures S2 and S3, Supporting Information), whereas drugs (such as Dox loaded by MoS_2 nanosheets) could be found in the whole cell, including the cell nucleus.[47] This difference suggests that drugs may enter the cell nucleus after they are released from their nanocarriers. Recently, Liang and co-workers demonstrated that Au nanoparticles smaller than 10 nm could enter the nucleus, whereas larger ones were only found in the cytoplasm.[56] In our study, we did not find MoS_2 nanosheets in the nucleus, even in the case of the 6 nm ones (Figure S3, Supporting Information), indicating that size is not the only factor determining whether nanoparticles can enter the cell nucleus. It is also expected that label-free method is more reliable for investigating the intracellular distribution of nanoparticles in vivo, since it is a direct means of visualizing them, whereas fluorescent molecules have a certain probability of detaching from nanoparticles due to cell–nanoparticle interactions.

We next quantified the internalization of MoS_2 nanosheets by live HeLa cells. Cells were incubated with MoS_2 nanosheets in DMEM (Dulbecco's modified eagle medium) for different amounts of time and were washed twice with PBS (phosphate-buffered saline) to remove MoS_2 from the culture medium. Afterward, the MoS_2/cells were imaged at the three time delays marked in Figure 4b. We quantified the amount of intracellular MoS_2 using the mean TA signal intensity per pixel in the cell regions for each field of view (FOV). The size of a cellular region was characterized by the total number of pixels in the protein channel above an intensity threshold, because proteins

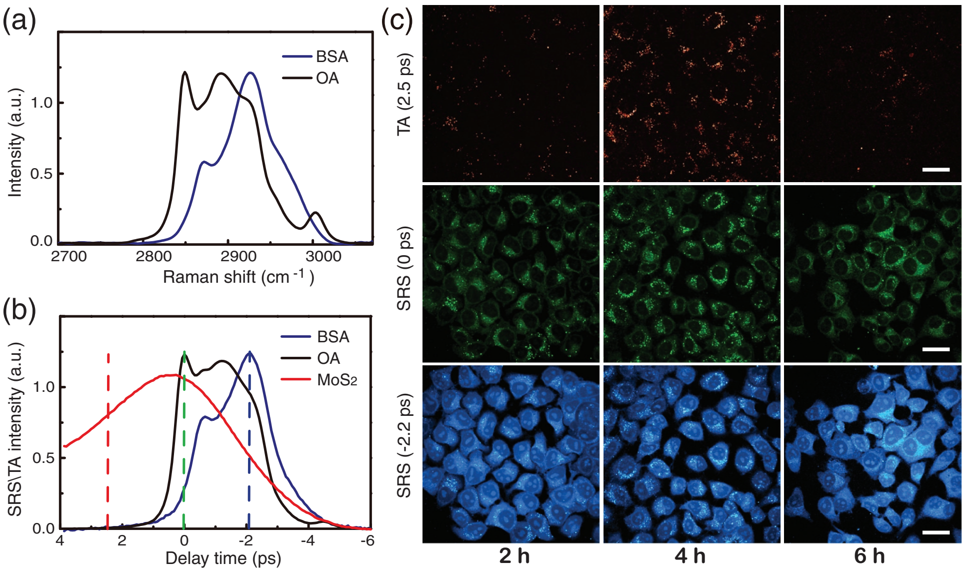

Figure 4. Dual-modal SRS/TA imaging of MoS_2 in live HeLa cells. a) Spontaneous Raman scattering spectra of bovine serum albumin (BSA) and oleic acid (OA). b) SRS spectra of BSA and OA as well as the time-resolved TA curve of MoS_2 nanosheets detected using spectral focusing mode. c) Representative SRS images of HeLa cells and TA images of intracellular MoS_2 detected at the three delay times marked in (b), showing the major contributions from MoS_2 (first row), lipids (second row), and proteins (third row). Scale bars: 30 µm.

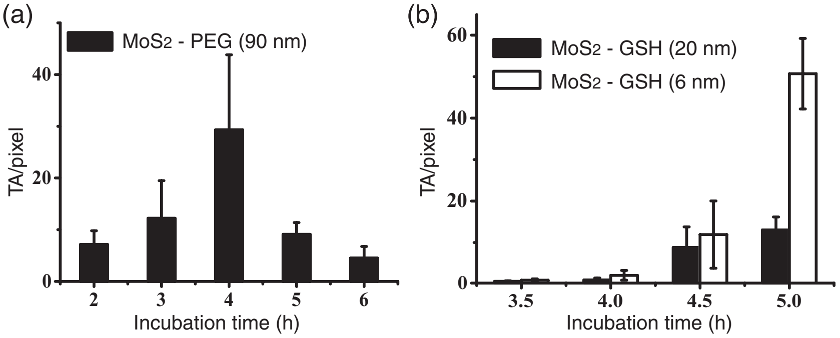

Figure 5. Quantitative measurements of the internalization dynamics of MoS_2 nanosheets in live HeLa cells. a) Large-sized MoS_2-PEG showed maximum uptake after ≈4 h of incubation time. b) Smaller-sized MoS_2-GSH particles showed different uptake dynamics.

distribute more evenly inside cells (Figure 4c, third row). At each incubation time, more than 50 FOVs were imaged and the mean TA/pixel values were analyzed to represent the amount of MoS_2 uptake. We took measurements at incubation time from 2 to 6 h at intervals of 1 h for MoS_2-PEG, and the statistical results are shown in **Figure 5**a. The internalization of MoS_2-PEG in HeLa cells was observed to reach a maximum value at 4 h and decrease afterward (Figure 5a). The large spatial heterogeneity caused large error bars, which indicates the importance of visualizing MoS_2 distribution in vivo.

We also studied the influence of nanoparticle size on uptake efficiency. Smaller MoS_2-GSH nanosheets incubated for 3.5–5 h were imaged and analyzed at 30 min intervals, as shown in Figure 5b. Our results indicated that smaller-sized MoS_2-GSH nanosheets have different internalization dynamics than the larger MoS_2-PEG particles, and in general, smaller particles tend to enter HeLa cells more efficiently. Furthermore, we found a significant amount of MoS_2-GSH aggregated outside the cells after 5 h of incubation. This effect was most obvious for the smallest MoS_2-GSH (6 nm) nanosheets (Figure S3, Supporting Information) but was absent for large-sized MoS_2-PEG (90 nm). This reflects a fast clearance of small MoS_2-GSH nanosheets from cells, which agrees with the rapid body clearance observed in photothermal cancer therapy.[49]

2.5. Colocalization of MoS_2 with Lipid Rich Organelles

To investigate the relative distribution of MoS_2 nanoparticles and cellular compartments in more detail, we imaged single cells with both sequential and parallel imaging methods (**Figure 6**). Current knowledge suggests that most nanostructures pass from endosomes to lysosomes after endocytosis, and eventually accumulate in late endosomes or lysosomes,[40,41,57–59] which are small organelles wrapped with lipid rich membranes. Noticing the "spectral" overlap between MoS_2 and lipids (Figure 4b), we applied a linear algorithm to decompose the raw images (taken at $\tau = 0$ ps and $\tau = 2.5$ ps) into MoS_2 and lipid channels based on prior knowledge of their spectral shapes. We found that the sequential imaging method usually generated "motion artifacts" due to the drift of intracellular compartments/nanoparticles between two sequential images taken at an interval of ≈1 s (Figure 6a). To eliminate these motion artifacts, we applied the parallel SRS/TA imaging technique introduced above to simultaneously image MoS_2 and lipids through the X and Y channels of the LIA. Using the parallel dual-modal imaging mode, we could see that MoS_2 and lipid rich organelles are indeed colocalized (Figure 6b). These lipid rich structures may represent endosomes and lysosomes; hence, the colocalization of MoS_2 and lipid droplets may further verify the hypothesis of the internalization mechanism and intracellular fate introduced above. Understanding the intracellular distribution and fate of nanoparticle drug carriers is necessary to elucidate their drug delivery mechanisms and is helpful for the rational design of novel nanoparticle drug delivery systems. Although we could not further distinguish endosomes and lysosomes at the current stage, our results indicate that this parallel imaging method is exceptional at studying detailed intracellular distribution or internalization dynamics and will benefit future studies on nanoparticle-assisted drug delivery.

3. Conclusions

In summary, we have developed a dual-modal SRS/TA microscopy technique to simultaneously image the biochemical components of cells and MoS_2 nanosheets. While SRS is sensitive to the intrinsic vibrational properties of biomolecules, TA is capable of capturing short-lived, transient optical properties that are not accessible with linear optical methods. Therefore, the combination of SRS and TA enables the study of interactions

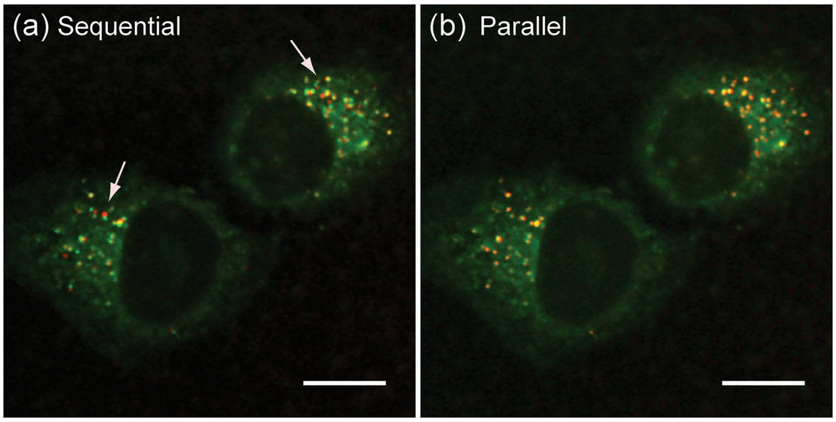

Figure 6. Colocalization of MoS_2 nanosheets with lipid droplets detected by dual-modal SRS/TA. a) The sequential imaging method generates "motion artifacts" indicated by the arrows. b) The parallel imaging method reveals the colocalization of MoS_2 with lipid droplets. Lipids are false colored in green and MoS_2 in red. Scale bars: 10 µm.

between biological systems and inorganic materials, especially most light-absorbing inorganic nanoparticles that do not emit one- or two-photon fluorescence. Moreover, both SRS and TA signal intensities are linearly proportional to the target sample concentrations, offering quantitative measurements of nanoparticle and biomolecule content. We believe our work provides a convenient way of imaging nanoparticle–cell systems in a label-free manner and will open up new research opportunities in nanomedicine.

4. Experimental section

Materials: All chemicals, unless otherwise specified, were purchased from Sigma-Aldrich. PEG and GSH polymers were purchased from PegBio, Suzhou, China. PBS, DMEM, and penicillin/streptomycin were purchased from HyClone. Fetal bovine serum (FBS) and trypsin were purchased from Gibco.

Synthesis and Modification of MoS_2-PEG: Larger-sized MoS_2 nanosheets were synthesized by the Morrison method.[47] Briefly, after 0.5 g of MoS_2 crystal was soaked in 0.5 mL of 1.6 M *n*-butyllithium solution in hexane for 2 d inside a nitrogen glove box, the MoS_2 sample was filtered and washed repeatedly with 80 mL hexane. Then, the intercalated MoS_2 sample was immediately removed from glove box and ultrasonicated in water for 1 h to obtain exfoliated MoS_2. Then, MoS_2 was centrifuged at 3000 rpm, and the supernatant was dialyzed against deionized water using membranes with a molecular weight cut-off (MWCO) of 14 kDa for 2 d to remove other residues. Finally, MoS_2 nanosheets dispersed in water were obtained.

For lipoic acid modified PEG (LA-PEG) functionalization, 10 mg of LA-PEG was added into 1 mg of MoS_2 nanosheets dispersed in 2 mL of water. After sonication for 20 min and stirring overnight, excess PEG was removed by centrifugal filtration with 100 kDa MWCO filters (Millipore), and the resulting sample was washed repeatedly using deionized water to obtain highly water-soluble MoS_2-PEG that was stored below 4 °C for future use.

Synthesis and Modification of MoS_2-GSH: Smaller MoS_2 nanosheets were synthesized in a modified bottom-up procedure.[49] In brief, 0.32 mL of hydrazine hydrate (50%) was added to 40 mL of methanol along with 10.4 mg of $(NH_4)_2MoS_4$ and 44 mg of PVP (polyvinyl pyrrolidone, 10 kDa) during ultrasonication. After 30 min, the solution was transferred to a Teflon-lined stainless steel autoclave and heated to 120 °C for 3 h. After the solution had cooled naturally, the as-prepared MoS_2 nanosheets were collected by evaporating the methanol and then dissolved in water.

To replace PVP and modify the MoS_2 nanosheets, 10-mass-fold of GSH was added to the solution during ultrasonication and stirred overnight. Excess GSH was removed by centrifugal filtration with 10 kDa MWCO filters (Millipore), and the resulting solution was washed repeatedly using deionized water. The condensed solution of MoS_2-GSH nanosheets was stored at 4 °C for future use.

Cell Culture and Incubation with MoS_2 Nanosheets: A human cervical cell line (HeLa cell) obtained from the American Type Culture Collection (ATCC) were cultured at 37 °C under an atmosphere of 5% CO_2. All cell culture-related reagents were purchased from Invitrogen. HeLa cells were grown in normal DMEM culture medium with 10% FBS and 1% penicillin/streptomycin. Cells were preseeded into 35 mm dishes and cultured for at least 24 h to make them completely adherent. When cells accounted for 70% of the volume of a dish, the normal DMEM culture medium was changed to 2 mL of DMEM containing 5 µL of MoS_2 and the resulting sample was incubated for different amounts of time. Before imaging, MoS_2 was removed from the medium by washing cells with PBS twice.

Imaging Parameters: The optical setup of the microscope system was described above in detail. The imaging speed used throughout the experiments was 2 µs per pixel, and each field of view contained 512 × 512 pixels. We used a 60× objective (Olympus, UPLSAPO 60XWIR, NA 1.2 water) for all cell imaging. Pump and probe laser powers of 10 mw each were used on the samples for MoS_2/cell imaging. All images were taken in transmission mode.

Supporting Information

Supporting Information is available from the Wiley Online Library or from the author.

Acknowledgements

L.Z. and S.S. contributed equally to this work. The authors are grateful for financial support from the National Key Research and Development Program of China (Grant Nos. 2016YFC0102100 and 2016YFA0301000); National Natural Science Foundation of China (Grant No. 81671725); Shanghai Rising Star program (Grant No. 15QA1400500); and Shanghai Action Plan for Scientific and Technological Innovation program (Grant No. 16441909200).

Note: Ref. 51 was corrected on April 20, 2017.

The authors declare no conflict of interest.

Keywords

biophotonics, multimodal imaging, stimulated Raman scattering, transient absorption microscopy

Received: January 18, 2017
Revised: March 1, 2017

[1] C. W. Freudiger, W. Min, B. G. Saar, S. Lu, G. R. Holtom, C. He, J. C. Tsai, J. X. Kang, X. S. Xie, *Science* **2008**, *322*, 1857.
[2] S. W. Hell, J. Wichmann, *Opt. Lett.* **1994**, *19*, 780.
[3] D. Y. Davydova, A. de la Cadena, D. Akimov, B. Dietzek, *Laser Photon. Rev.* **2016**, *10*, 62.
[4] C. Schwarz, F. Milan, T. Hahn, M. Reichenberger, S. Kümmel, A. Köhler, *Adv. Funct. Mater.* **2014**, *24*, 6439.
[5] X. Zhang, M. B. Roeffaers, S. Basu, J. R. Daniele, D. Fu, C. W. Freudiger, G. R. Holtom, X. S. Xie, *ChemPhysChem* **2012**, *13*, 1054.
[6] D. Fu, F. K. Lu, X. Zhang, C. Freudiger, D. R. Pernik, G. Holtom, X. S. Xie, *J. Am. Chem. Soc.* **2012**, *134*, 3623.
[7] C. Cao, D. Zhou, T. Chen, A. M. Streets, Y. Huang, *Anal. Chem.* **2016**, *88*, 4931.
[8] L. Wei, F. Hu, Z. Chen, Y. Shen, L. Zhang, W. Min, *Acc. Chem. Res.* **2016**, *49*, 1494.
[9] M. Ji, D. A. Orringer, C. W. Freudiger, S. Ramkissoon, X. Liu, D. Lau, A. J. Golby, I. Norton, M. Hayashi, N. Y. Agar, G. S. Young, C. Spino, S. Santagata, S. Camelo-Piragua, K. L. Ligon, O. Sagher, X. S. Xie, *Sci. Transl. Med.* **2013**, *5*, 201ra119.
[10] M. Ji, S. Lewis, S. Camelo-Piragua, S. H. Ramkissoon, M. Snuderl, S. Venneti, A. Fisher-Hubbard, M. Garrard, D. Fu, A. C. Wang, J. A. Heth, C. O. Maher, N. Sanai, T. D. Johnson, C. W. Freudiger, O. Sagher, X. S. Xie, D. A. Orringer, *Sci. Transl. Med.* **2015**, *7*, 309ra163.
[11] F. K. Lu, D. Calligaris, O. I. Olubiyi, I. Norton, W. Yang, S. Santagata, X. S. Xie, A. J. Golby, N. Y. Agar, *Cancer Res.* **2016**, *76*, 3451.
[12] M. C. Wang, W. Min, C. W. Freudiger, G. Ruvkun, X. S. Xie, *Nat. Methods* **2011**, *8*, 135.

[13] D. Fu, Y. Yu, A. Folick, E. Currie, R. V. Farese, T. H. Tsai, X. S. Xie, M. C. Wang, *J. Am. Chem. Soc.* **2014**, *136*, 8820.
[14] D. Fu, J. Zhou, W. S. Zhu, P. W. Manley, Y. K. Wang, T. Hood, A. Wylie, X. S. Xie, *Nat. Chem.* **2014**, *6*, 614.
[15] T. Chen, Y. Huang, *Small* **2015**, *11*, 4998.
[16] A. Shimizu, T. Morimae, *Phys. Rev. Lett.* **2005**, *95*, 090401.
[17] M. S. Devadas, Z. Li, G. V. Hartland, *J. Phys. Chem. Lett.* **2014**, *5*, 2910.
[18] T. Chen, S. Chen, J. Zhou, D. Liang, X. Chen, Y. Huang, *Nanoscale* **2014**, *6*, 10536.
[19] C. R. Carey, Y. Yu, M. Kuno, G. V. Hartland, *J. Phys. Chem. C* **2009**, *113*, 19077.
[20] T. Chen, F. Lu, A. M. Streets, P. Fei, J. Quan, Y. Huang, *Nanoscale* **2013**, *5*, 4701.
[21] Y. Jung, M. N. Slipchenko, C. H. Liu, A. E. Ribbe, Z. Zhong, C. Yang, J. X. Cheng, *Phys. Rev. Lett.* **2010**, *105*, 217401.
[22] L. Tong, Y. Liu, B. D. Dolash, Y. Jung, M. N. Slipchenko, D. E. Bergstrom, J. X. Cheng, *Nat. Nanotechnol.* **2012**, *7*, 56.
[23] B. Gao, G. V. Hartland, L. Huang, *ACS Nano* **2012**, *6*, 5083.
[24] J. Li, W. Zhang, T. F. Chung, M. N. Slipchenko, Y. P. Chen, J. X. Cheng, C. Yang, *Sci. Rep.* **2015**, *5*, 12394.
[25] L. Huang, G. V. Hartland, L.-Q. Chu, R. M. Luxmi, R. M. Feenstra, C. Lian, K. Tahy, H. Xing, *Nano Lett.* **2010**, *10*, 1308.
[26] B. Gao, G. Hartland, T. Fang, M. Kelly, D. Jena, H. G. Xing, L. Huang, *Nano Lett.* **2011**, *11*, 3184.
[27] S. Murphy, L. Huang, *J. Phys. Cond. Matter* **2013**, *25*, 144203.
[28] B. A. Ruzicka, L. K. Werake, H. Zhao, S. Wang, K. P. Loh, *Appl. Phys. Lett.* **2010**, *96*, 173106.
[29] P. M. Cal, F. Sieglitz, F. M. Santos, C. Parente Carvalho, A. Guerreiro, J. B. Bertoldo, U. Pischel, P. M. Gois, G. J. Bernardes, *Chem. Commun.* **2017**, *53*, 368.
[30] L. L. Zheng, C. M. Li, S. J. Zhen, Y. F. Li, C. Z. Huang, *Nanoscale* **2016**, *8*, 18635.
[31] B. Barlag, O. Beutel, D. Janning, F. Czarniak, C. P. Richter, C. Kommnick, V. Goser, R. Kurre, F. Fabiani, M. Erhardt, J. Piehler, M. Hensel, *Sci. Rep.* **2016**, *6*, 31601.
[32] S. H. Alamudi, R. Satapathy, J. Kim, D. Su, H. Ren, R. Das, L. Hu, E. Alvarado-Martínez, J. Y. Lee, C. Hoppmann, E. Peña-Cabrera, H.-H. Ha, H.-S. Park, L. Wang, Y.-T. Chang, *Nat. Commun.* **2016**, *7*, 11964.
[33] L. J. Macpherson, E. E. Zaharieva, P. J. Kearney, M. H. Alpert, T. Y. Lin, Z. Turan, C. H. Lee, M. Gallio, *Nat. Commun.* **2015**, *6*, 10024.
[34] J. Zhang, F. Cheng, J. Li, J. J. Zhu, Y. Lu, *Nano Today* **2016**, *11*, 309.
[35] W. Zhou, D. Li, C. Xiong, R. Yuan, Y. Xiang, *ACS Appl. Mater. Interfaces* **2016**, *8*, 13303.
[36] N. Bossert, D. de Bruin, M. Gotz, D. Bouwmeester, D. Heinrich, *Sci. Rep.* **2016**, *6*, 37897.
[37] H. Chen, Z. Wang, S. Zong, L. Wu, P. Chen, D. Zhu, C. Wang, S. Xu, Y. Cui, *ACS Appl. Mater. Interfaces* **2014**, *6*, 17526.
[38] G. B. Braun, T. Friman, H. B. Pang, A. Pallaoro, T. Hurtado de Mendoza, A. M. Willmore, V. R. Kotamraju, A. P. Mann, Z. G. She, K. N. Sugahara, N. O. Reich, T. Teesalu, E. Ruoslahti, *Nat. Mater.* **2014**, *13*, 904.
[39] H. Yang, C. Lou, M. Xu, C. Wu, H. Miyoshi, Y. Liu, *Int. J. Nanomed.* **2011**, *6*, 2023.
[40] G. Sahay, W. Querbes, C. Alabi, A. Eltoukhy, S. Sarkar, C. Zurenko, E. Karagiannis, K. Love, D. Chen, R. Zoncu, Y. Buganim, A. Schroeder, R. Langer, D. G. Anderson, *Nat. Biotechnol.* **2013**, *31*, 653.
[41] J. Gilleron, W. Querbes, A. Zeigerer, A. Borodovsky, G. Marsico, U. Schubert, K. Manygoats, S. Seifert, C. Andree, M. Stoter, H. Epstein-Barash, L. Zhang, V. Koteliansky, K. Fitzgerald, E. Fava, M. Bickle, Y. Kalaidzidis, A. Akinc, M. Maier, M. Zerial, *Nat. Biotechnol.* **2013**, *31*, 638.
[42] N. Rapoport, R. Gupta, Y. S. Kim, B. E. O'Neill, *J. Controlled Release* **2015**, *206*, 153.
[43] J. Chen, C. Liu, D. Hu, F. Wang, H. Wu, X. Gong, X. Liu, L. Song, Z. Sheng, H. Zheng, *Adv. Funct. Mater.* **2016**, *26*, 8715.
[44] D. Li, W. Xiong, L. Jiang, Z. Xiao, H. R. Golgir, M. Wang, X. Huang, Y. Zhou, Z. Lin, J. Song, S. Ducharme, L. Jiang, J. F. Silvain, Y. Lu, *ACS Nano* **2016**, *10*, 3766.
[45] T. Liu, C. Wang, W. Cui, H. Gong, C. Liang, X. Shi, Z. Li, B. Sun, Z. Liu, *Nanoscale* **2014**, *6*, 11219.
[46] L. Cheng, J. Liu, X. Gu, H. Gong, X. Shi, T. Liu, C. Wang, X. Wang, G. Liu, H. Xing, W. Bu, B. Sun, Z. Liu, *Adv. Mater.* **2014**, *26*, 1886.
[47] T. Liu, C. Wang, X. Gu, H. Gong, L. Cheng, X. Shi, L. Feng, B. Sun, Z. Liu, *Adv. Mater.* **2014**, *26*, 3433.
[48] A. H. Loo, A. Bonanni, M. Pumera, *Analyst* **2016**, *141*, 4654.
[49] T. Liu, Y. Chao, M. Gao, C. Liang, Q. Chen, G. Song, L. Cheng, Z. Liu, *Nano Res.* **2016**, *9*, 3003.
[50] I. Moreels, K. Lambert, D. Smeets, M. D. De, T. Nollet, J. C. Martins, F. Vanhaecke, A. Vantomme, C. Delerue, G. Allan, *ACS Nano* **2009**, *3*, 3023.
[51] R. He, Y. Xu, L. Zhang, S. Ma, X. Wang, D. Ye, M. Ji, *Optica* **2017**, *4*, 44.
[52] D. Fu, G. Holtom, C. Freudiger, X. Zhang, X. S. Xie, *J. Phys. Chem. B* **2013**, *117*, 4634.
[53] P. D. Cunningham, K. M. McCreary, B. T. Jonker, *J. Phys. Chem. Lett.* **2016**, *7*, 5242.
[54] D. Lagarde, L. Bouet, X. Marie, C. R. Zhu, B. L. Liu, T. Amand, P. H. Tan, B. Urbaszek, *Phys. Rev. Lett.* **2014**, *112*, 047401.
[55] C. de Mello Donegá, M. Bode, A. Meijerink, *Phys. Rev. B* **2006**, *74*, 085320.
[56] S. Huo, S. Jin, X. Ma, X. Xue, K. Yang, A. Kumar, P. C. Wang, J. Zhang, Z. Hu, X. J. Liang, *ACS Nano* **2014**, *8*, 5852.
[57] Y. Zhang, V. Krieger, M. Hensel, *J. Vis. Exp.* **2015**, *95*, e52058.
[58] A. Panarella, M. G. Bexiga, G. Galea, O. N. Ed, A. Salvati, K. A. Dawson, J. C. Simpson, *Sci. Rep.* **2016**, *6*, 28865.
[59] X. Ma, Y. Wu, S. Jin, Y. Tian, X. Zhang, Y. Zhao, L. Yu, X. J. Liang, *ACS Nano* **2011**, *5*, 8629.